HHS Public Access

Author manuscript

IEEE Trans Med Imaging. Author manuscript; available in PMC 2023 July 01.

Published in final edited form as:

IEEE Trans Med Imaging. 2022 July ; 41(7): 1724–1734. doi:10.1109/TMI.2022.3147497.

High-speed balanced-detection visible-light optical coherence tomography in the human retina using subpixel spectrometer calibration

Ian Rubinoff,
Department of Biomedical Engineering at Northwestern University, Evanston, IL, 60208

David A. Miller,
Department of Biomedical Engineering at Northwestern University, Evanston, IL, 60208

Roman Kuranov,
Department of Biomedical Engineering at Northwestern University, Evanston, IL, 60208

Opticent Health, Evanston, IL, 60201

Yuanbo Wang,
Opticent Health, Evanston, IL, 60201

Raymond Fang,
Department of Biomedical Engineering at Northwestern University, Evanston, IL, 60208

Nicholas J. Volpe,
Department of Ophthalmology at Northwestern University, Chicago, IL, 60611

Hao F. Zhang
Department of Biomedical Engineering at Northwestern University, Evanston, IL, 60208

Abstract

Increases in speed and sensitivity enabled rapid clinical adoption of optical coherence tomography (OCT) in ophthalmology. Recently, visible-light OCT (vis-OCT) achieved ultrahigh axial resolution, improved tissue contrast, and provided new functional imaging capabilities, demonstrating the potential to improve clinical care further. However, limited speed and sensitivity caused by the high relative intensity noise (RIN) in supercontinuum lasers impeded the clinical adoption of vis-OCT. To overcome these limitations, we developed balanced-detection vis-OCT (BD-vis-OCT), which uses two calibrated spectrometers to cancel RIN and other noises. We analyzed the RIN to achieve robust subpixel calibration between the two spectrometers and showed that BD-vis-OCT reduced the A-line noise floor by up to 20.5 dB. Metrics comparing signal-to-noise-ratios showed similar image qualities across multiple reference arm powers, a hallmark of operation near the shot-noise limit. We imaged healthy human retinas at an A-line rate of 125 kHz and a field-of-view up to 10 mm × 4 mm. We found that BD-vis-OCT revealed retinal anatomical features previously obscured by the noise floor.

ianrubinoff2022@u.northwestern.edu .

Keywords

optical coherence tomography; relative intensity noise; supercontinuum laser; balanced detection; retina

I. Introduction

Optical coherence tomography (OCT) images the living human retina noninvasively at micrometer-scale volumetric resolutions [1, 2]. Since its first demonstration in the early 1990s, OCT has rapidly become the clinical imaging standard for diagnosing, treating, and monitoring nearly all retinal diseases [2, 3]. The clinical adoption of OCT can be partially attributed to technical advancements in imaging speed and sensitivity. Development of spectral-domain OCT enabled high-speed imaging at 100s of kHz with increased sensitivity [2–5]. Traditionally, spectral-domain OCT has operated in the near-infrared (NIR) wavelength range (800 nm-1300 nm).

The recent development of visible-light OCT (vis-OCT) [6], which operates near 500 nm – 600 nm, has shown promise for providing valuable information not available in NIR OCT. Using shorter wavelengths, vis-OCT enables an axial resolution < 2 μm [6–9], at least 2-fold higher than clinical NIR systems. Hence vis-OCT revealed or enhanced retinal structures previously inaccessible by NIR OCT by taking advantage of its high axial resolution and increased tissue scattering contrast. For example, recent studies have found that vis-OCT can delineate Bruch's membrane (BM) [8–10], a structural origin of macular degeneration, and the inner plexiform layer (IPL) sublayers [11, 12], which contains scattering information from dendritic connections that may be a biomarker for glaucoma. Additionally, vis-OCT achieved retinal oximetry by analyzing spectral contrast between oxygenated and deoxygenated blood [13], opening a new window for functional retinal imaging.

Although vis-OCT enhances structural and functional information in the retina, it has unique limits that hamper its clinical adoption. Perhaps the most significant limitation is the light source. Unlike NIR-OCTs, which use low-noise superluminescent diodes (SLDs), vis-OCT relies on supercontinuum lasers. Supercontinuum lasers have intrinsic power fluctuations referred to as relative intensity noise (RIN) [6, 14, 15]. After the Fourier transform, the RIN increases the image background's average amplitude (noise floor) and variation (noise). The increased noise floor amplitude degrades vis-OCT's image contrast, while the increased noise variation increases the uncertainty of vis-OCT's pixel amplitudes. RIN can be suppressed by increasing the exposure time of the spectrometer's camera (decreasing A-line rate) to average out intensity fluctuations [14]. Therefore, vis-OCT researchers often limited A-line rates near or below 30 kHz in human retinal imaging [8–11, 16, 17]. Such low A-line rates induce two challenges. First, head and eye motions [9, 18] make optical alignment, large field-of-view (FOV) volumetric imaging, and image registrations for frame averaging more challenging. Second, prolonged imaging time increases light exposure in the eye. Although within the ANSI laser safety standards [17], the visible-light illumination may be distracting and uncomfortable, inducing additional eye motions. Eye motions and

high RIN reduce vis-OCT's ability to resolve minute retinal anatomical features, such as IPL sublayers and BM, and measure functional parameters, such as oximetry. Song et al. reported vis-OCT retinal imaging at an A-line rate of 100 kHz [19]; however, they limited the illumination bandwidth to 35 nm to increase power density, which degraded axial resolution to ~ 5 μm and did not solve the RIN problem. Recent work using an all-normal dispersion (ANDi) fiber [20, 21] showed a supercontinuum laser with low RIN. However, its output was only demonstrated between 670 nm – 1390 nm, where the SLDs and swept-source lasers within the same spectral range also had shown very low RIN.

Until now, there has been no good solution to achieve high A-line rate, maintain broad spectral bandwidth, and suppress RIN at the same time in vis-OCT. Addressing the noise floor is particularly challenging because it reduces image contrast and, unlike noise variation, it cannot be removed by frame averaging or filtering. Our solution is to develop a balanced-detection (BD) vis-OCT, which uses two calibrated spectrometers to cancel noises (including RIN) [3, 22, 23]. BD has been well-demonstrated in swept-source OCT [2, 3], where two single-element detectors record interference sweeping through the entire bandwidth to reject influences from light source energy instability. BD was also tested in spectrometer-based OCT systems [23–28]. A comprehensive study by Bradu et al. found no noise floor reduction, partially attributed to poor calibration between the two spectrometers [24]. Other demonstrations also showed limited success, where researchers routinely reported 3–6 dB increases in signal intensity but no significant reduction in the noise floor [23, 25–28]. Because BD equally splits the interference signals into two separate paths before being recombined, the reported improvement in signal amplitude is not obvious when compared with a single spectrometer detection without splitting the interference signal [24]. One study circumvented the calibration problem by interleaving detection of fringes in time on the same spectrometer [28], but degraded the effective A-line rate by 50%. Reducing RIN should be a key goal of BD but is particularly constrained by the inability to calibrate two spectrometers precisely.

Recently, Kho et al. [29] reported that excess noise (dominated by RIN) from a supercontinuum source is spectrally encoded on the spectrometer. This allowed for accurate pixel-to-wavelength mapping using only the RIN. Since the goal of BD is to subtract RIN commonly measured across two spectrometers, we hypothesize that it is optimal to calibrate spectrometers using the RIN itself. This new calibration differs from previous calibrations [23–25, 27], which make overly simplified assumptions that careful optical alignment, finding overlap in the OCT fringes or background spectra, or linear wavenumber (k) interpolation can achieve efficient noise reduction in BD SD-OCT.

In this work, we show for the first time that creating a subpixel map between two spectrometers using RIN correlation, polynomial fitting such map, and using the map to interpolate OCT fringes greatly improves the efficiency of BD and significantly reduces the OCT noise floor. First, we developed BD-vis-OCT based on a Mach-Zehnder interferometer and calibrated two spectrometers using the spectrally-encoded RIN. After calibrating two spectrometers with subpixel accuracy, we subtracted their interference fringes to reject the RIN. Subsequently, we investigated BD performance as a function of calibration errors and found that subpixel accuracy is necessary for optimal RIN rejection. We validated RIN

rejection in a retinal phantom at multiple reference arm power levels by tuning spectrometer camera gain and found up to 20.5 dB reduction in the noise floor. In addition, we imaged the retinas of five healthy human volunteers at 125 kHz A-line rate using BD SD-OCT. BD vis-OCT revealed anatomical features previously obscured by the noise floor, opening a new window for high-speed SD-OCT ophthalmic imaging using high RIN light sources.

II. Methods and Materials

A. Experimental Setup

Fig. 1A illustrates the BD-vis-OCT system based on a modified Mach-Zehnder interferometer (MZI) configuration. The MZI's transmission-based configuration minimizes the number of fiber couplers in the light paths to reduce losses. A supercontinuum laser (SCL, SuperK 78 MHz EXW-6, NKT Photonics, Denmark) delivered light to a multistage filter set consisting of a dichroic mirror (DM1, DMSP650, Thorlabs, NJ), polarizer (P, WP25M-VIS, Thorlabs), bandpass filter (BPF, FF01–560/94–25, Semrock, NY), and spectral shaping filter (Hoya B-460, Edmund Optics, NJ). We coupled the light into a 10:90 fiber coupler (FC1, TW560R3A2, Thorlabs). The 10% output of FS1 delivered light to the sample arm (Fig. 1A, bottom). A collimating lens (CL) collimated a 2.5-mm diameter beam incident on a galvanometer scanner (Cambridge Technology, MA). A two-lens telescopic system (L1 and L2) with a 3:2 magnification ratio delivered 240 μW to the eye. Meanwhile, a red diode laser (DL, LPS-675-FC, Thorlabs) delivered 5 μW to the eye for fixation. We separated the fixation light from the vis-OCT path using a dichroic mirror (DM2, 3114–666, Alluxa, CA). A microelectromechanical scanner (MS, Mirrorcle, Richmond, CA) scanned a 'star-shaped' fixation pattern on the retina during vis-OCT imaging. The 90% output of FC1 was input to a transmission-type reference arm, consisting of a polarization controller (PC), a fiber delay line (FD), and an adjustable air delay (AD) line. The AD and dispersion compensation (DC) matched the double-pass path length in the free space part of the sample arm, while the FD matched the double-pass fiber path length in the sample arm. Backscattered light from the sample arm and transmitted light from the reference arm interfered in a 50:50 fiber coupler (FC2, TW560R5A2, Thorlabs). We collected the interfered light from both output arms using two spectrometers (SRA and SRB, Blizzard SR, Opticent Inc.,) which offer a maximum A-line rate of 135 kHz using a 1D CCD camera (OctoPlus, Teledyne e2v). SRA covers 509.1 nm to 613.7 nm and SRB covers 507.5 nm to 613.1 nm. The BPF slightly reduces the usable range to 513 nm to 607 nm. We subtracted the SRA detection from the SRB detection for BD. Due to manufacturing imperfection, the splitting ratio of FC2 was slightly asymmetric, as shown in Fig. 1B, which did not significantly compromise the BD performance. SRA and SRB have alignment differences as indicated by their different wavenumber (k) [30] spacings in Fig. 1C. The k-spacings show that the spectrometer alignments are nonlinear with respect to pixel index and nonlinear with respect to each other, making hardware-based calibration impractical and software-based calibration non-trivial. We measured an *in vivo* axial resolution of 1.7 μm with SRB alone (single detection, or SD) and with SRA & SRB for BD (see Supplementary Materials)[1].

[1]Supplementary Materials are available in the supporting documents/multimedia tab. Further references to Supplementary Materials are in the same location.

At 1-mm imaging depth, SRA & SRB have signal roll-offs of −4.3 dB and −3.6 dB, respectively, and a combined BD (SRB-SRA) signal roll-off of −4.0 dB (Fig. 1D). At a 125 kHz A-line rate and minimal camera amplification, we measured sensitivities of 73.1 dB and 99.6 dB near the zero-delay for SRB and BD, respectively. System performance for *in vivo* and *ex vivo* imaging are shown in Section III.

B. Balanced Detection Processing

Fig. 2 shows the flowchart detailing the steps for BD from acquisition to image reconstruction. Briefly, we acquired A-lines in SRA and SRB simultaneously. In pre-processing, we scaled the spectrum in SRA by its ratio with that in SRB to digitally match their DC shapes. This did not enhance image quality but allowed for a more unbiased comparison of image quality metrics considering any deviations from an ideal 50:50 splitting ratio (Fig. 1B). Then, we removed the DC components from the respective fringes. After pre-processing the fringes, we applied a calibration map generated by the maximum RIN correlations between SRA and SRB [29]. We fitted a third-order polynomial to the map to reduce undersampling artifacts caused by the finite pixel number of the camera. The calibration and its performance are detailed later in Section III-A. We used the calibration map to interpolate the fringes from SRA to linear with respect to SRB. After calibration, we subtracted the respective fringes between SRB and SRA. Finally, we performed traditional OCT image reconstruction, including k-space interpolation, compensation for dispersion mismatch, and the Fourier transform.

C. Phantom Eye Imaging

We imaged a phantom eye (OCT Model Eye, Rowe Technical Design) using a rectangular scan consisting of 512 A-lines × 64 B-scans at an A-line rate of 125 kHz (7.7 μs exposure time, 0.3 μs readout time). The total acquisition time was 0.26 seconds. We imaged at the highest and lowest camera gain levels.

D. Human Imaging

We imaged the eyes of four healthy volunteers between 25 and 47 years of age. The imaging procedure was approved by the Northwestern University institutional review board (IRB), and volunteers provided informed consent before imaging. Imaging was performed at an A-line rate of 125 kHz (7.7 μs exposure time, 0.3 μs readout time) using the highest camera gain. Vis-OCT illumination light power was no higher than 240 μW on the cornea. We scanned multiple patterns: small FOV with a 4 mm × 4 mm scanning range and 512 A-lines × 256 B-scans (total acquisition time: 1 second); medium FOV with a 7 mm × 4 mm scanning range and 1024 A-lines × 256 B-scans (total acquisition time: 2 seconds); large FOV with a 10 mm × 4 mm scanning range and 1024 A-lines × 256 B-scans (total acquisition time: 2 seconds); and high-density speckle reduction (HDSR) [9] with either a 12 mm × 3 mm or 8 mm × 3 mm scanning range and 32768 A-lines × 16 B-scans (total acquisition time: 4 seconds). HDSR scans consisted of 16 scans orthogonal to the B-scan axis [9]. All respective scans in this work were acquired within 4 seconds or less.

E. Image Quality Metrics

Noise floor amplitude and variation, which increase with RIN, degrade image quality. We adopted three commonly-used metrics to compare image quality between SD and BD.

OCT image sensitivity was previously defined as the ratio of the signal to the noise floor [2]. Here, we use a similar metric called peak-signal-to-noise-floor-ratio

$$PSNFR = 20\ \log_{10}\frac{A_{sig_m}}{A_{floor}}, \tag{1}$$

where A_{sig_m} is the maximum amplitude of the selected signal and A_{floor} is the average amplitude of the noise floor near A_{sig_m}. PSNFR describes the range where a signal can be differentiated from A_{floor}. Increased PSNFR results in higher imaging sensitivity and contrast between the signal and noise floor. Previous reports showed A_{sig_m} is biased when it is not sufficiently larger than A_{floor}, thereby biasing PSNFR [31]. We found empirically in our images that this bias becomes small when PSNFR > 10 dB. Rather than make assumptions about the exact influence of this bias, we measured PSNFR in regions with PSNFR > 10 dB.

Next, we measured image peak-signal-noise-ratio [32]

$$PSNR = 20\ \log_{10}\frac{A_{sig_m}}{\sigma_{floor}}, \tag{2}$$

where σ_{floor} is the standard deviation of the noise floor near A_{sig_m}. PSNR highlights pixel uncertainty relative to the peak signal. Due to the potential bias in A_{sig_m}, we measured PSNFR in the same brightly reflecting regions as PSNFR.

Finally, we measured contrast-to-noise ratio [32]

$$CNR = 10\ \log_{10}\frac{A_{sig} - A_{floor}}{\sqrt{\sigma_{sig}^2 + \sigma_{floor}^2}}, \tag{3}$$

where A_{sig} is the selected signal amplitude (not necessarily maximum); and σ_{sig} is the standard deviation of the selected signal. CNR highlights limitations from both contrast and pixel uncertainty. For a weak vis-OCT signal in SD, $A_{sig} - A_{floor}$ could be close to zero or negative, yielding an extremely negative (< −10 dB) or complex CNR. We considered these cases as ‘noise floor limited’.

III. Results

A. Spectrometer Noise Analysis

We compared noises in the spectrometers before and after BD calibration in the 1D CCD camera array. Figs. 3A–3C show the noises at camera pixel index 500 acquired across 100

continuous camera exposures. Fig. 3A shows noises in SRA (orange) and SRB (blue) before the calibration procedure. The standard deviation (σ, [arb. units]) of noises is 160.6 for SRA and 160.4 for SRB. The noises do not overlap, which is a result of their alignment differences. The difference is quantified by their correlation coefficient (CC) of 0.49. Fig. 3B plots the same noises after calibration. After calibration, the noises overlap almost identically with a CC of 0.99. Fig. 3C plots the difference between the noises from SRA and SRB before and after calibration. The noise subtraction without calibration has a significantly higher standard deviation (σ = 157.6) than after calibration (σ = 19.6).

We validated these trends for each pixel in the spectrometer. Fig. 3D plots the σ of noises from SRA and SRB and the σ of their difference before and after calibration for 5000 camera exposures. The average σ across all pixels (neglecting edges of the camera where there is no light) is 131.1 for SRA and 123.9 for SRB. The average σ across all pixels after taking the difference of the spectrometers is 21.7 with calibration and 133.1 without calibration. The average CC between SRA and SRB is 0.46 before calibration and 0.99 after calibration. As shown in Fig. 3D, calibration effectively reduces noise across all camera pixels (all wavelengths). Furthermore, there is a spectral dependence in noises before calibration (orange and blue lines) and in their difference without calibration (yellow line), indicating the spectral dependence of RIN [6]. After calibration, the noises are mostly flat across all pixels (wavelengths), indicating an effective RIN rejection. We note a small oscillation in the calibrated noise difference. This is associated with aliasing by the finite pixel sampling of the camera. This artifact is mostly suppressed by fitting a third-order polynomial to the calibration map (Fig. 3E) to estimate continuous subpixel mapping. In the Supplementary Materials, we show the impact of fitting the calibration map on noise subtraction.

As seen in previous BD SD-OCT results [23–28], hardware and software calibrations are non-trivial and susceptible to errors. We show that accurate subpixel calibration is necessary for optimal noise rejection. To assess the impact of a potential miscalibration, we added constant subpixel shifts to each pixel in the calibration map in Fig. 3E. Fig. 3F plots the correlation between noises in SRA and SRB as a function of pixel shift. The purple line shows the average CC across all pixels when the shifted calibration map is applied, and the yellow line shows the average CC when no calibration is applied (CC = 0.46). The optimal calibration map yields a CC = 0.99 at 0 pixel shift. Meanwhile, noise correlation decays exponentially for nonzero pixel shifts. The average CC drops to 0.96 at ±0.5 pixel shift, 0.87 at ±1 pixel shift, and 0.64 at ±3 pixel shift.

Fig. 3G plots the noise suppression by taking the ratio of average σ from SRA and the σ difference of SRA and SRB $\left(\frac{\sigma_{SRA}}{\sigma_{SRB}-\sigma_{SRA}}\right)$. When this ratio is 1, the average σ after BD is the same as SRA. The purple line shows the average noise suppression across all pixels when the shifted calibration map is applied. The yellow line shows the average noise suppression when no calibration is applied (noise suppression ratio = 0.99, which is noisier than SRA alone). The optimal calibration map yields a noise suppression ratio of 6.0 at 0 pixel shift. The average noise suppression ratio is 3.3 at ±0.5 pixel shift, 2.1 at ±1 pixel shift, and 1.2 at ±3 pixel shift. The majority (67%) of noise suppression inefficiency occurs when

the pixel shift is < 1, and about half (45%) of the noise suppression inefficiency occurs when the pixel shift < 0.5. This means that the subpixel calibration accuracy demonstrated in our work is critical for balanced detection to be effective. Such high sensitivity to subpixel shift is further emphasized by the average CC, where only a 3% drop in the CC at ± 0.5 pixel shift (Fig. 3F) corresponds to a 45% drop in noise suppression (Fig. 3G).

As a comparison, Kuo et al. [23] performed hardware and software-based calibration for BD SD-OCT by finding overlapping features in the spectra detected by the two spectrometers. They estimated ~ 40% inefficiency in their noise subtraction and did not demonstrate any noise floor reduction. Such a method is not necessarily sensitive to subpixel differences or nonlinearities between the spectrometers. The spectrometer noise analysis presented here provides a quantitative explanation of and solution for the inefficiencies of BD SD-OCT. We note that the potential miscalibrations tested here (constant pixel shift across camera array) are likely overly simplified. In reality, the nonlinear nature of spectrometer alignment (e.g., Fig. 1C and also reported by Kuo et al.) can introduce additional non-linear pixel errors across the camera array, making the subpixel sensitivities shown here conservative estimations.

B. Imaging Phantom Eyeball

We imaged a phantom eyeball to assess BD-vis-OCT retinal imaging in a well-controlled environment. We compared SD and BD images using the spectrometer camera's highest and lowest gains and measured PSNFR, PSNR, and CNR. Reference arm powers were set to ~ 67% of the saturation limit of the camera.

Figs. 3A & 3B show SD and BD B-scans (five-times averaging) of the phantom at the highest manufacturer-specified camera gain. The images are plotted on the same contrast scales (2% of pixel outliers at extremes removed, square root scale, normalized between 0 and 1). All vis-OCT images in this work are plotted on this contrast scale. Fig. 3C plots A-lines from the regions highlighted by the red and green dashed lines in Figs. 3A and 3B, respectively. The peak near 200 μm depth from BD (green line) is ~ 6 dB higher than that from SD (red line), consistent with the addition of two fringes from SRA and SRB. The noise floor (near 100 μm depth) is 9.5 dB lower for BD than SD.

To measure PSNFR and PSNR in the phantom eye, we used the homogeneous brightly reflecting region at the top of the phantom (Figs. 3A & 3B) to minimize the bias potential bias. We averaged five adjacent A-lines and automatically used the maximum amplitude at the selected bright reflection as A_{sig_m}. We used the average of a 20-pixel (depth) × 20-pixel (lateral) window centered 70 pixels above A_{sig_m} as A_{floor}. We measured PSNFR and PSNR for A-lines 25 through 425 (of 512), avoiding the edges of the image, which were too close to the zero-delay to measure the noise floor accurately. To measure CNR in the phantom retina, we used the average of a 20-pixel (depth) × 20-pixel (lateral) region below the bright line as A_{sig} and the average of a 20-pixel (depth) × 20-pixel (lateral) window centered 70 pixels above the bright line at the same lateral location as A_{floor}.

Image metrics for Figs. 4A & 4B are summarized in Table I. After BD, PSNFR increases by 14.8 dB and PSNR increases by 14.6 dB. For boxes labeled 1–3, after BD, CNR increases from ~ 1 dB or less to 3–4 dB.

Figs. 4D & 4E show SD and BD B-scans (five-times B-scan averaging) of the phantom at the lowest manufacturer-specified spectrometer camera gain. Reducing the camera gain increased its photon detection capacity. Reaching the same detection amplitude as the highest camera gain (shown by noise floor amplitude ~75 dB in Figs. 4C & 4F) while maintaining the same sample arm power required increasing reference arm power, which also increased contribution of RIN. While SD failed to resolve the phantom structure clearly, BD fully revealed all the structural details. Fig. 4C plots the A-lines from the locations highlighted by the red and green dashed lines in Figs. 4A and 4B, respectively. The peak near 200 μm depicts the bright layer on the top of the phantom, which is is ~ 5 dB higher for BD (green line) than SD (red line). The expected BD increase is 6 dB from the addition of the two interference fringes; the lower value (5 dB vs. 6 dB) is associated with noise bias in the SD. The noise floor (near 100 μm) is ~ 20.5 dB lower for BD than SD.

Image metrics for Figs. 4D & 4E are also summarized in Table I. Using BD, PSNFR increases by 25.3 dB and PSNR increases by 25.6 dB. For boxes labeled 1–3, after BD, CNR increases from noise floor limited or very negative to 3–4 dB.

In spectral domain OCT, assuming reference arm power is much greater than sample arm power, A-line intensity scales linearly with reference arm power [2, 23]. For a shot-noise limited system, A-line noise variance scales linearly with the reference arm power; for a RIN-dominated system, it scales with the square of the reference arm power [23]. Therefore, PSNFR and PSNR are sensitive to reference arm power increases in a RIN-dominated system but are insensitive to reference arm power increases in a shot-noise limited system [14, 23, 24]. For SD, image quality metrics are highly sensitive to the camera gain-determined reference arm power. The lower gain level has 8.6 dB lower PSNFR and 8.8 dB lower PSNR. The majority of this difference can be attributed to RIN. Comparatively, BD is significantly less sensitive to the camera gain-determined reference arm power (the lower gain level has 1.9 dB higher PSNFR and 2.2 dB higher PSNR). Small changes to PSNFR and PSNR in response to a near 3-fold increase in RIN suggests that BD-vis-OCT removes nearly all RIN and operates near the shot-noise limit. The slightly better performance of the lower amplification level may be attributed to the slightly lower electronic noises or increased reference arm power.

C. Imaging Human Retina with Small Field-of-View

Fig. 5 shows the small FOV scan located near the fovea of the right eye of a healthy, 47-year-old male volunteer (Eye 1). Figs. 5A & 5B show *en-face* images for SD and BD, respectively. We generated the *en-face* images by taking the mean intensity projection of the retinal volume after cropping out the first 20 pixels along the depth direction. The red and green dashed boxes in Figs. 5A & 5B highlight regions that are magnified by Figs. 5C and 5D, respectively. Fig. 5D reveals small vessels (highlighted by green stars) buried in the noise floor with SD in Fig. 5C (highlighted by red stars). Figs. 5E & 5F show B-scans (registered and averaged five times) at the locations highlighted by the red and

green dashed lines in Figs. 5A & 5B, respectively. Comparing with SD (Fig. 5E), where the high noise floor obscures the anatomical details [10, 33], the BD resolves them. To highlight the qualitative difference in structural visibility between SD and BD, we overlaid A-lines (log scale) on their respective locations in Figs 5E and 5F. A-line 1 highlights a blood vessel at its respective location in the SD (red A-line) and BD (green A-line). For SD, the signal within the blood vessel is buried in the noise floor. Meanwhile, the reduced noise floor in BD reveals the characteristic blood signal decay [34, 35]. The attenuation is visible across the entire depth of the vessel. A-line 2 highlights the retinal anatomical layers resolved by SD and BD, respectively. BD reveals the inner plexiform layer (IPL) sublayers, which has three distinct bright laminations and is a promising biomarker for glaucoma [11, 12]. In SD image and A-line, IPL is invisible.

To measure PSNFR and PSNR in the human retina, we identified brightly reflecting regions at the internal limiting membrane (ILM). We averaged 5 adjacent A-lines and automatically used the maximum amplitude at the selected bright reflection as A_{sig_m}. Since such bright reflections are sparse in the human retina, we measured PSNFR and PSNR only in discrete regions. We used the average of a 20-pixel (depth) × 20-pixel (lateral) window centered 50 pixels above A_{sig_m} as A_{floor}. To measure CNR in the human retina, we used the average of a 20-pixel (depth) × 20-pixel (lateral) region in the nerve fiber layer (NFL) as A_{sig} and the average of a 20-pixel (depth) × 20-pixel (lateral) window centered 50 pixels above the ILM at the same lateral location as A_{floor}.

We measured PSNFR and PSNR at an ILM reflection (highlighted by red and green arrows in Figs. 5E & 5F, respectively). We measured CNRs in the RNFL highlighted by the red and green boxes labeled 1 and 2. Image metrics for Figs. 5E & 5F (Eye 1) and all volunteers (Eyes 2–5) are summarized in Table II. In Figs. 5E & 5F, PSNFR increases by 15.1 dB and PSNR increases by 15.1 dB. CNR in boxes 1 & 2 increase from negative to 4.4 dB and 3.7 dB, respectively.

There are minimal motion artifacts in the small FOV volume. We did not perform any registrations for the *en face* projections. At 125-kHz A-line rate, the small FOV volumes were acquired in 1 second, overcoming many fundamental limitations from eye motions, where, for example, involuntary saccades occur on the order of 1 Hz [18]. Additional images with small FOV from other volunteers are shown in Supplementary Materials.

D. Imaging Human Retina with Medium Field-of-View

Fig. 6 compares SD and BD vis-OCT image with medium FOV from the left eye of a 24-year-old male volunteer (Eye 2). En face projections (Figs. 6A and 6B) cover the fovea and optic disc (OD) in a single scan with minimal motions. In the BD image (Fig. 6B), as compared with SD, vessels from the OD to the fovea are visible at the capillary level thanks to the improved optical contrast within the visible-light spectral range. Figs. 6C and 6D are magnified views of the areas highlighted by the red and green dashed boxes in Figs. 6A and 6B, respectively, where capillaries are better visualized by BD.

Figs. 6E and 6F show B-scans (registered and averaged five times) from respective locations highlighted by the red and green dashed in Figs. 6A and 6B. Similar to the small FOV B-scans, BD reveals the retinal anatomical layers with much higher contrast than SD. In previous work by Rubinoff et al. [9], we showed that B-scans acquired at an A-line rate of 25 kHz could not be registered and directly averaged without significant blurring. Here, we show that with a 125 kHz A-line rate and near the same scanning range, five B-scans can be registered and averaged with nearly no blurring. We previously limited vis-OCT's A-line rate at 25 kHz to reduce the influence of RIN and increase image quality in human imaging. BD achieved comparable image quality at a 5-fold increased A-line rate. In Figs. 6E and 6F, we overlay two A-lines (log scale) that highlight retinal structures and a blood vessel at their respective locations (highlighted 1 & 2). We measured PSNFR and PSNR at the regions highlighted by the red and green arrows, respectively. For SD, PSNFR and PSNR are 16.1 dB and 28.6 dB, respectively. For BD, PSNFR and PSNR are 31.4 dB and 43.8 dB, respectively. PSNFR and PSNR increased by 15.3 dB and 15.2 dB, respectively. We measured CNR in the areas highlighted by the red and green boxed regions labeled 1 and 2 in Figs. 6E and 6F. In Fig. 6E, CNRs are − 6.7 dB in box 1 and −9.7 dB in box 2. In Fig. 6F, CNRs are are 3.3 dB in box 1 and 3.8 dB in box 2. Additional images with medium FOV are shown in Supplementary Materials.

E. Imaging Human Retina with Large Field-of-View with High-Density Speckle Reduction

Figs. 7A and 7B respectively show en-face SD and BD vis-OCT images from Eye 2 with large FOV and Figs. 7C and 7D respectively show high-density speckle reduction (HDSR) [9] SD and BD B-scan image from the positions highlighted by red and green dashed lines in Figs 7A and 7B, respectively. The large FOV scan enables vis-OCT to provide an unprecedented view of the retina beyond the macula and optic disc while exhibiting minimal motions thanks to the 125-kHz A-line rate. We combined the large FOV scan with an HDSR scan. A benefit of the HDSR scan is that it can combine dense A-line scanning, speckle reduction, and wide scanning range without registrations [9]. Dense A-line scanning can also help reduce fringe washout from the scanner across a long scanning range. At a σ125 kHz A-line rate, we can increase HDSR A-line density without sacrificing the total scanning time. Here, we acquired HDSR B-scans with 32768 A-lines (0.26 s per B-scan) and laterally averaged them 32 times, allowing many more averages than in the medium FOV (five averages) while scanning a larger range. The red and green dashed boxes (labeled 1–3) in Figs. 7C and 7D highlight three retinal regions in the HDSR B-scan image, and their magnified views are shown below the B-scan images. Following the pattern in Figs. 5 & 6, BD, but not SD, reveals retinal layers (boxes 1 & 2) and blood vessels (boxes 2 & 3, highlighted by stars) across the retina. As seen in Fig. 7D and magnified by green boxes 1 & 2, IPL, RPE, and BM (see Figs. 5 & 6) are delineated across nearly the entire scanning range. vis-OCT imaging across a large FOV can be useful for mapping structures like IPL, RPE, and BM, providing new information for the diagnosis, monitoring, and treatment of blinding diseases. An additional example of an HDSR scan is available in Supplementary Materials.

IV. Discussion

We demonstrated BD in vis-OCT for the first time after a subpixel calibration of two spectrometers using the RIN itself. We showed in a phantom retina that BD reduces the noise floor up to 20.5 dB and reaches nearly identical image quality metrics under both highest and lowest camera gains, despite RIN being significantly at the lowest camera gain. This implies that BD is highly effective in removing high levels of RIN and that vis-OCT can afford shorter spectrometer exposure times, higher A-line rates, and cheaper light sources. Based on our *in vivo* results, we anticipate that BD-vis-OCT can reach A-line rates higher than 200 kHz, although one potential limitation is fringe washout caused by optical scanning.

We overcame discrete sampling limitations by fitting our calibration map with a third-order polynomial. This enabled subpixel calibration accuracy, giving an average CC = 0.99 between noises in the two spectrometers. Calibration accuracy may be further improved by either increasing the camera sampling density (pixel number) or reducing the k-spacing (smaller bandwidth), although additional technical complications may have diminishing benefits, given the high CC already found in the fitting approach.

We investigated the importance of subpixel calibration accuracy in BD for the first time. We showed a steep decay in noise suppression efficiency for even small pixel inaccuracies (Fig. 3G). For example, 67% of potential noise reduction is lost for average calibration errors of < 1 pixel, and 45% of potential noise reduction is lost for average calibration errors of < 0.5 pixels. Practical hardware tolerances, human errors, and wavelength-dependent nonlinearities make hardware-based calibrations infeasible and other software-based calibrations extremely challenging and inefficient. The high calibration accuracy required for complete RIN rejection better explains why previous demonstrations of BD SD-OCT were generally ineffective at reducing the noise floor and overall signal quality, despite increasing signal 3–6 dB. It also informs researchers the upper limitations of RIN rejection and the methods and tolerances necessary to achieve in BD SD-OCT.

In our phantom measurements, we found small image quality enhancements using the lower camera amplification compared with the higher camera amplification. This may be associated with lower electronic noises in the lower amplification, or perhaps the increased dynamic range of the detector, which merits a future, systemic investigation. Since each camera's amplification settings are set by the manufacturer and are not necessarily ubiquitous, we recommend that researchers optimize the unique settings of their cameras to maximize PSNFR and SNFR.

We found *in vivo* in five volunteers aged 25–47 that PSNFR and PSNR increases are near those found in the retinal phantom (~14–15 dB). We found CNR increases from negative to up to 4.4 dB. Most importantly, we found that retinal features entirely obscured by RIN in SD are revealed by BD. Based on roll-off measurements and image comparisons, we did not observe any significant signal decay, artifacts, or resolution loss that may be attributed to poor calibration. RIN was previously suppressed in vis-OCT by reducing the A-line rate to perform increased temporal averaging of the interference fringe. When

combined with the distraction and potential discomfort of a visible-light beam, low speed is perhaps the critical limiting factor for translating vis-OCT to the clinics. BD enables high-speed vis-OCT without significantly sacrificing image quality, resolution, or spectroscopic bandwidth. Additionally, supercontinuum lasers are more costly than SLDs, and technology improvements to reduce RIN in supercontinuum lasers may add additional costs. BD-vis-OCT significantly reduces the influence of RIN, permits high-speed, high-quality human imaging, and imposes fewer performance requirements on supercontinuum lasers, all of which may bring down the overall vis-OCT cost. Although we focus on vis-OCT here, it is not the only OCT technology where BD is applicable. Other OCTs use supercontinuum sources to achieve broad bandwidths to increase axial resolution [36], or operate in the far-infrared range for deep penetration [37].

The recent development of ANDi fiber supercontinuum lasers [20] presented a positive step forward in low RIN supercontinuum-based OCT. However, its demonstration for OCT is limited to the NIR wavelength range and is not yet commercially available. Unlike introducing a new source, BD requires no new laser technologies or expertise and is immediately compatible with all existing high-RIN supercontinuum sources across any wavelength range. Robust and simple subpixel calibration enables using two spectrometers with different hardware alignments, removing a major technical hurdle that previously prevented noise rejection. Since calibration only requires spectrometer detection of reference arm power, it can be performed without additional alignments, making operation feasible in a closed box in a clinical setting by non-technical experts. Since calibration can be performed after each acquisition, BD is robust against any hardware misalignments over time. As scanning speeds continuously increase, less temporal averaging will increase RIN, perhaps even in a low RIN ANDi supercontinuum source. BD maintains at least equivalent performances despite significantly increased RIN, which we validated (Fig. 4) by minimizing camera amplification. Our RIN-rejection methods enable supercontinuum light sources to be suitable for much broader OCT applications beyond visible-light spectral range.

V. Conclusion

We developed BD-vis-OCT based on an MZI. Using BD, we demonstrated high-quality human retinal imaging at an A-line rate of 125 kHz, the fastest with vis-OCT so far. In a phantom eyeball, we demonstrated at high RIN levels that PSNFR increases by up to 25.3 dB and PSNR up to 25.6 dB. We demonstrated such increases *in vivo* by up to 15.3 dB and 15.2 dB, respectively. For both the phantom and *in vivo* images, CNRs were mostly negative or noise floor limited in SD, but increased up to 3–4 dB after BD. Most of these increases came from the reduction of RIN. Qualitatively, BD revealed more structural features *in vivo* than SD. We anticipate that BD will enable broad and immediate clinical applications of vis-OCT and other OCTs using supercontinuum sources.

Supplementary Material

Refer to Web version on PubMed Central for supplementary material.

Acknowledgments

The authors thank Dr. Lisa Beckmann for helpful discussions. This work was supported in part by NIH grants R01EY026078, R01EY029121, R01EY028304, R01EY019949, U01EY033001, and R44EY026466.

This paragraph of the first footnote will contain the date on which you submitted your paper for review. The authors were supported by National Institutes of Health (NIH) grants R01EY019949, R01EY026078, R01EY028304, R01EY029121, and R44EY02646.

References

[1]. Huang D et al. , “Optical Coherence Tomography,” (in English), Science, vol. 254, no. 5035, pp. 1178–1181, Nov 22 1991, doi: DOI 10.1126/science.1957169. [PubMed: 1957169]

[2]. de Boer JF, Leitgeb R, and Wojtkowski M, “Twenty-five years of optical coherence tomography: the paradigm shift in sensitivity and speed provided by Fourier domain OCT [Invited],” (in English), Biomed Opt Express, vol. 8, no. 7, pp. 3248–3280, Jul 1 2017, doi: 10.1364/Boe.8.003248. [PubMed: 28717565]

[3]. Wojtkowski M, “High-speed optical coherence tomography: basics and applications,” (in English), Appl Optics, vol. 49, no. 16, pp. D30–D61, Jun 1 2010, doi: 10.1364/Ao.49.000d30.

[4]. Nassif N et al. , “In vivo human retinal imaging by ultrahigh-speed spectral domain optical coherence tomography,” (in English), Opt Lett, vol. 29, no. 5, pp. 480–482, Mar 1 2004, doi: Doi 10.1364/Ol.29.000480. [PubMed: 15005199]

[5]. Choma MA, Sarunic MV, Yang CH, and Izatt JA, “Sensitivity advantage of swept source and Fourier domain optical coherence tomography,” (in English), Opt Express, vol. 11, no. 18, pp. 2183–2189, Sep 8 2003, doi: 10.1364/Oe.11.002183. [PubMed: 19466106]

[6]. Shu X, Beckmann L, and Zhang HF, “Visible-light optical coherence tomography: a review,” (in English), J Biomed Opt, vol. 22, no. 12, Dec 2017, doi: Artn 121707 10.1117/1.Jbo.22.12.121707.

[7]. Beckmann L et al. , “Longitudinal deep-brain imaging in mouse using visible-light optical coherence tomography through chronic microprism cranial window,” (in English), Biomedical Optics Express, vol. 10, no. 10, pp. 5235–5250, Oct 1 2019, doi: 10.1364/Boe.10.005235. [PubMed: 31646044]

[8]. Chong SP, Zhang TW, Kho A, Bernucci MT, Dubra A, and Srinivasan VJ, “Ultrahigh resolution retinal imaging by visible light OCT with longitudinal achromatization,” (in English), Biomed Opt Express, vol. 9, no. 4, pp. 1477–1491, Apr 1 2018, doi: 10.1364/Boe.9.001477. [PubMed: 29675296]

[9]. Rubinoff I et al. , “Speckle reduction in visible-light optical coherence tomography using scan modulation,” (in English), Neurophotonics, vol. 6, no. 4, Oct-Dec 2019, doi: ARTN 041107 10.1117/1.NPh.6.4.041107.

[10]. Zhang TW, Kho AM, Yiu G, and Srinivasan VJ, “Visible Light Optical Coherence Tomography (OCT) Quantifies Subcellular Contributions to Outer Retinal Band 4,” (in English), Transl Vis Sci Techn, vol. 10, no. 3, Mar 2021, doi: 10.1167/tvst.10.3.30.

[11]. Zhang T, Kho AM, and Srinivasan VJ, “In vivo Morphometry of Inner Plexiform Layer (IPL) Stratification in the Human Retina With Visible Light Optical Coherence Tomography,” (in English), Frontiers in Cellular Neuroscience, Original Research vol. 15, no. 147, 2021-April-29 2021, doi: 10.3389/fncel.2021.655096.

[12]. Ghassabi Z et al. , “In Vivo Sublayer Analysis Of Human Retinal Inner Plexiform Layer Obtained By Visible-Light Optical Coherence Tomography,” bioRxiv, p. 2021.01.08.425925, 2021, doi: 10.1101/2021.01.08.425925.

[13]. Yi J, Wei Q, Liu WZ, Backman V, and Zhang HF, “Visible-light optical coherence tomography for retinal oximetry,” (in English), Opt Lett, vol. 38, no. 11, pp. 1796–1798, Jun 1 2013, doi: 10.1364/Ol.38.001796. [PubMed: 23722747]

[14]. Jensen M et al. , “Noise of supercontinuum sources in spectral domain optical coherence tomography,” (in English), J Opt Soc Am B, vol. 36, no. 2, pp. A154–A160, Feb 1 2019, doi: 10.1364/Josab.36.00a154.

[15]. Shin S, Sharma U, Tu HH, Jung W, and Boppart SA, “Characterization and Analysis of Relative Intensity Noise in Broadband Optical Sources for Optical Coherence Tomography,” (in English), Ieee Photonic Tech L, vol. 22, no. 14, pp. 1057–1059, Jul 15 2010, doi: 10.1109/Lpt.2010.2050058.

[16]. Zhang TW, Kho AM, and Srinivasan VJ, “Improving visible light OCT of the human retina with rapid spectral shaping and axial tracking,” (in English), Biomed Opt Express, vol. 10, no. 6, pp. 2918–2931, Jun 1 2019, doi: 10.1364/Boe.10.002918. [PubMed: 31259062]

[17]. Chen SY, Shu X, Nesper PL, Liu WZ, Fawzi AA, and Zhang HF, “Retinal oximetry in humans using visible-light optical coherence tomography [Invited],” (in English), Biomed Opt Express, vol. 8, no. 3, pp. 1415–1429, Mar 1 2017, doi: 10.1364/Boe.8.001415. [PubMed: 28663838]

[18]. Martinez-Conde S, Macknik SL, and Hubel DH, “The role of fixational eye movements in visual perception,” (in English), Nat Rev Neurosci, vol. 5, no. 3, pp. 229–240, Mar 2004, doi: 10.1038/nrn1348. [PubMed: 14976522]

[19]. Song W et al. , “Visible light optical coherence tomography angiography (vis-OCTA) facilitates local microvascular oximetry in the human retina,” Biomed Opt Express, vol. 11, no. 7, pp. 4037–4051, 2020/07/01 2020, doi: 10.1364/BOE.395843. [PubMed: 33014584]

[20]. Rao D SS et al. , “Shot-noise limited, supercontinuum-based optical coherence tomography,” Light: Science & Applications, vol. 10, no. 1, p. 133, 2021/06/28 2021, doi: 10.1038/s41377-021-00574-x.

[21]. Genier E et al. , “Ultra-flat, low-noise, and linearly polarized fiber supercontinuum source covering 670–1390 nm,” (in English), Opt Lett, vol. 46, no. 8, pp. 1820–1823, Apr 15 2021, doi: 10.1364/Ol.420676. [PubMed: 33857078]

[22]. Podoleanu AG, “Unbalanced versus balanced operation in an optical coherence tomography system,” (in English), Appl Optics, vol. 39, no. 1, pp. 173–182, Jan 1 2000, doi: Doi 10.1364/Ao.39.000173.

[23]. Kuo WC, Lai CM, Huang YS, Chang CY, and Kuo YM, “Balanced detection for spectral domain optical coherence tomography,” (in English), Opt Express, vol. 21, no. 16, pp. 19280–19291, Aug 12 2013, doi: 10.1364/Oe.21.019280. [PubMed: 23938845]

[24]. Bradu A and Podoleanu AG, “Fourier domain optical coherence tomography system with balance detection,” (in English), Opt Express, vol. 20, no. 16, pp. 17522–17538, Jul 30 2012, doi: 10.1364/Oe.20.017522. [PubMed: 23038305]

[25]. Kuo WC, Lai YS, Lai CM, and Huang YS, “Balanced detection spectral domain optical coherence tomography with a multiline single camera for signal-to-noise ratio enhancement,” (in English), Appl Optics, vol. 51, no. 24, pp. 5936–5940, Aug 20 2012, doi: 10.1364/Ao.51.005936.

[26]. Black AJ and Akkin T, “Polarization-based balanced detection for spectral-domain optical coherence tomography,” (in English), Appl Optics, vol. 54, no. 24, pp. 7252–7257, Aug 20 2015, doi: 10.1364/Ao.54.007252.

[27]. Bo E, Liu XY, Chen S, Yu XJ, Wang XH, and Liu LB, “Spectral-domain optical coherence tomography with dual-balanced detection for auto-correlation artifacts reduction,” (in English), Opt Express, vol. 23, no. 21, pp. 28050–28058, Oct 19 2015, doi: 10.1364/Oe.23.028050. [PubMed: 26480462]

[28]. Hyeon MG, Kim HJ, Kim BM, and Eom TJ, “Spectral domain optical coherence tomography with balanced detection using single line-scan camera and optical delay line,” (in English), Opt Express, vol. 23, no. 18, pp. 23079–23091, Sep 7 2015, doi: 10.1364/Oe.23.023079. [PubMed: 26368412]

[29]. Kho AM, Zhang TW, Zhu J, Merkle CW, and Srinivasan VJ, “Incoherent excess noise spectrally encodes broadband light sources,” (in English), Light-Sci Appl, vol. 9, no. 1, Oct 6 2020, doi: ARTN 172 10.1038/s41377-020-00404-6.

[30]. Rubinoff I et al. , “Spectrally dependent roll-off in visible-light optical coherence tomography,” (in English), Opt Lett, vol. 45, no. 9, pp. 2680–2683, May 1 2020, doi: 10.1364/Ol.389240. [PubMed: 32356845]

[31]. Baumann B et al. , “Signal averaging improves signal-to-noise in OCT images: But which approach works best, and when?,” (in English), Biomed Opt Express, vol. 10, no. 11, pp. 5755–5775, Nov 1 2019, doi: 10.1364/Boe.10.005755. [PubMed: 31799045]

[32]. Szkulmowski M, Gorczynska I, Szlag D, Sylwestrzak M, Kowalczyk A, and Wojtkowski M, "Efficient reduction of speckle noise in Optical Coherence Tomography," (in English), Opt Express, vol. 20, no. 2, pp. 1337–1359, Jan 16 2012, doi: 10.1364/Oe.20.001337. [PubMed: 22274479]

[33]. Drexler W, Morgner U, Ghanta RK, Kartner FX, Schuman JS, and Fujimoto JG, "Ultrahigh-resolution ophthalmic optical coherence tomography," (in English), Nat Med, vol. 7, no. 4, pp. 502–507, Apr 2001, doi: Doi 10.1038/86589. [PubMed: 11283681]

[34]. Veenstra C, Kruitwagen S, Groener D, Petersen W, Steenbergen W, and Bosschaart N, "Quantification of total haemoglobin concentrations in human whole blood by spectroscopic visible-light optical coherence tomography," (in English), Sci Rep-Uk, vol. 9, Oct 22 2019, doi: ARTN 15115 10.1038/s41598-019-51721-9.

[35]. Huang YY et al. , "Optical Coherence Tomography Detects Necrotic Regions and Volumetrically Quantifies Multicellular Tumor Spheroids," (in English), Cancer Res, vol. 77, no. 21, pp. 6011–6020, Nov 1 2017, doi: 10.1158/0008-5472.Can-17-0821. [PubMed: 28904062]

[36]. Wang TA, Chan MC, Lee HC, Lee CY, and Tsai MT, "Ultrahigh-resolution optical coherence tomography/angiography with an economic and compact supercontinuum laser," (in English), Biomed Opt Express, vol. 10, no. 11, pp. 5687–5702, Nov 1 2019, doi: 10.1364/Boe.10.005687. [PubMed: 31799040]

[37]. Israelsen NM et al. , "Real-time high-resolution mid-infrared optical coherence tomography," (in English), Light-Sci Appl, vol. 8, Jan 23 2019, doi: ARTN 11 10.1038/s41377-019-0122-5.

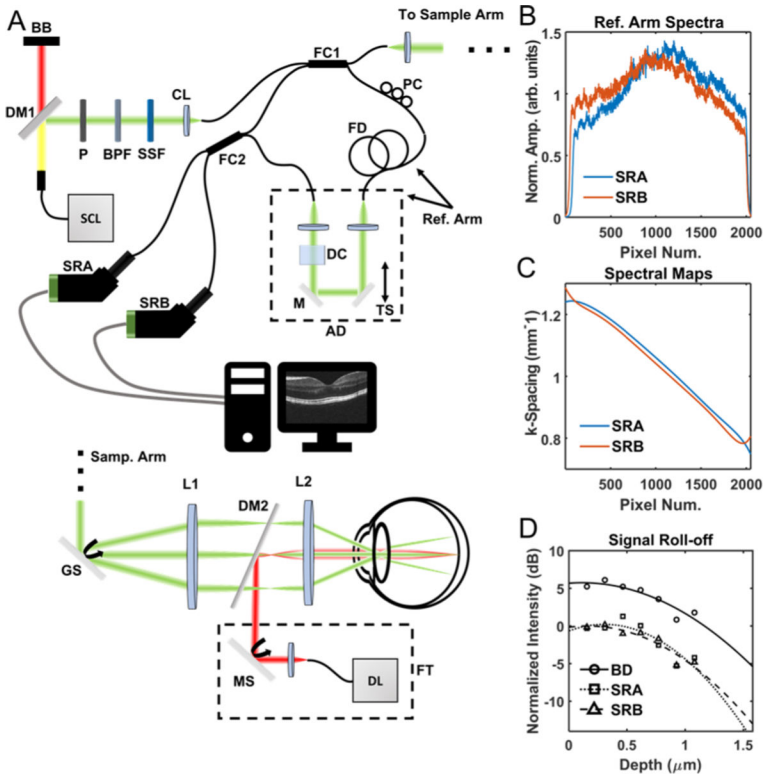

Fig. 1.

(A) Schematic of BD-vis-OCT system. SCL: supercontinuum laser; DM: dichroic mirror; BB: beam block; P: polarizer; BPF: bandpass filter; SSF: spectral shaping filter; CL: collimating lens; PC: polarization controller; FC: fiber coupler; FD: fiber delay; TS: translation stage; M: mirror; DC: dispersion compensation; AD: air delay; SRA: spectrometer A; SRB: spectrometer B; GS: galvanometric scanner; L: lens; MS: microelectromechanical scanner; DL: diode laser; FT: fixation target; (B) reference arm spectra; (C) spectrometer wavenumber (k) maps; (D) Signal roll-offs normalized with respect to the first depth measurement in SRB. Circle, square, and triangle show actual measurements for SRA, SRB and balanced detection (BD); corresponding lines show best fits.

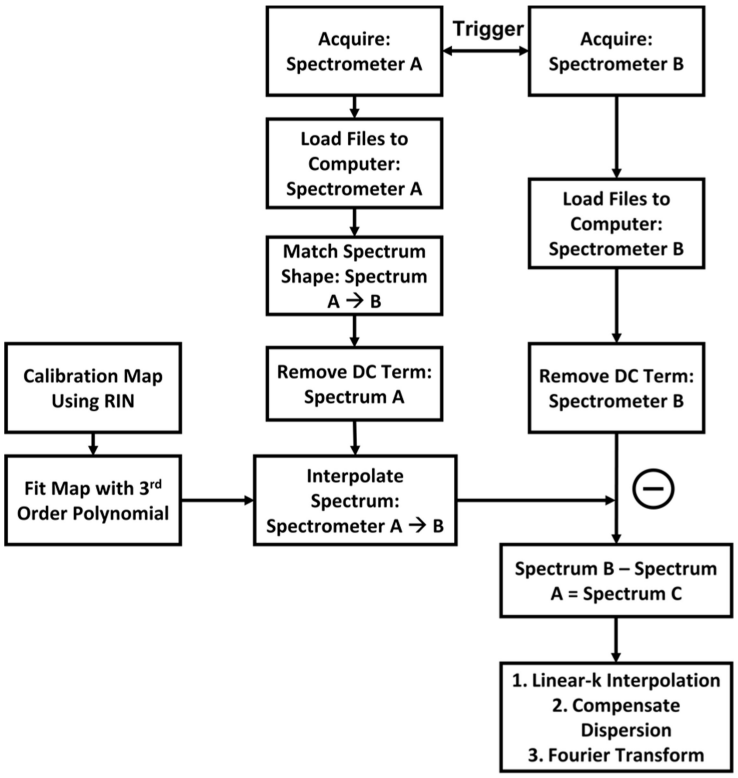

Fig. 2.
Flowchart for BD vis-OCT. The sequence follows arrows from top to bottom.

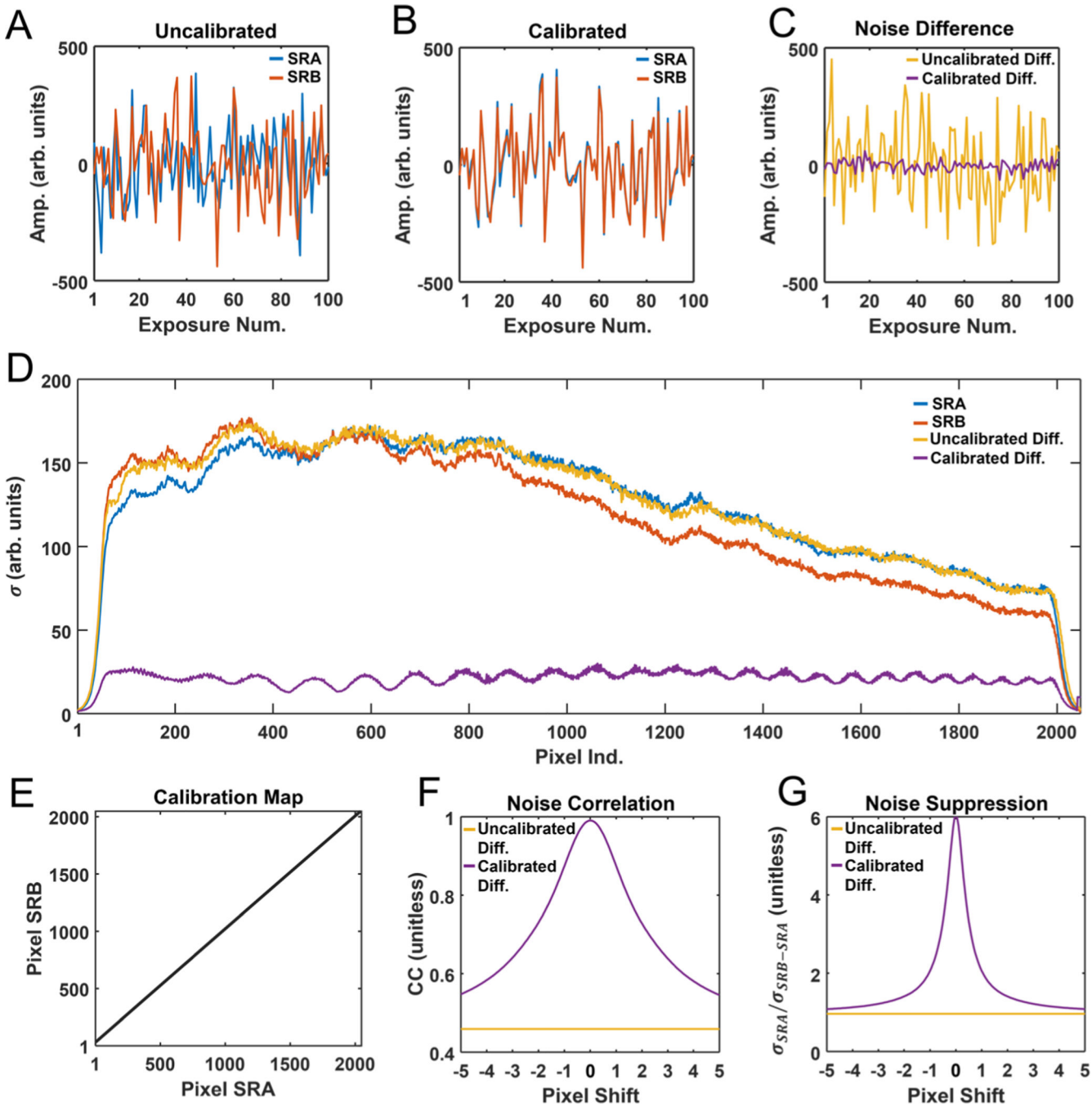

Fig. 3.

Spectrometer noises in 100 continuous camera exposures for the camera pixel 500 without calibration (A), with calibration (B), and after subtraction between spectrometer B (SRB) and A (SRA) (C); (D) Standard deviations of noises across the entire camera array; (E) Calibration map relating pixels in SRB to pixels in SRA. The map is nonlinear and displayed after fitting by a third-order polynomial; (F) Correlation coefficient as a function of shifting the map in (E). (G) Average ratio of standard deviation between SRA and the difference of

SRA and SRB as a function of shifting the map in (E). Higher ratio indicates better noise suppression. In (F) & (G), pixel shift = 0 represents the optimal calibration map.

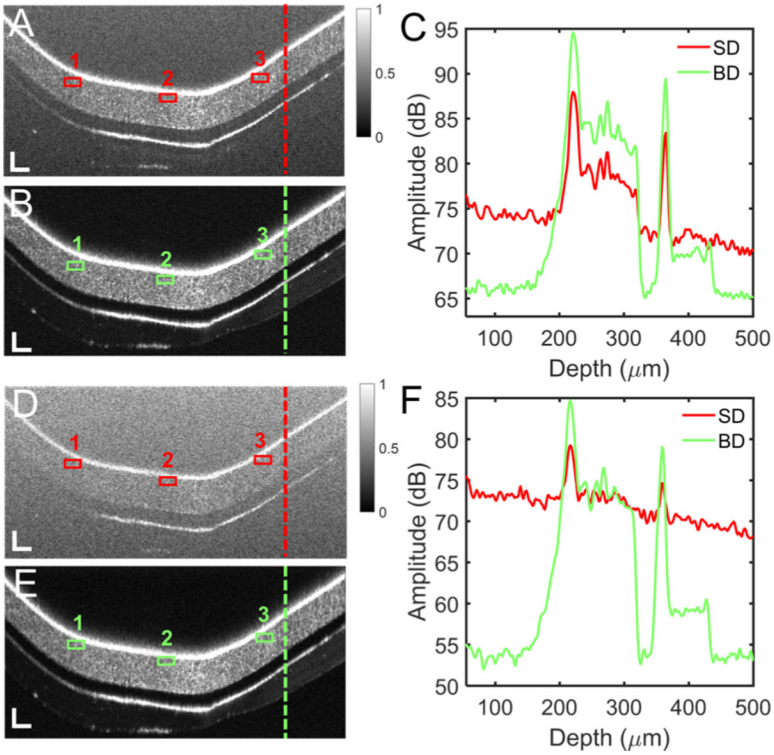

Fig. 4.

(A) Single detection and (B) balanced detection B-scans of phantom eye at lowest camera amplification level. Red and green boxes highlight measurement locations of CNR. Red and green dashed lines highlight locations of A-lines plotted in (C); (D-F) Following same layout as (A-C) but for maximum camera amplification level. B-scans magnified to show detail. Scale bars 50 μm (vertical) × 225 μm (horizontal).

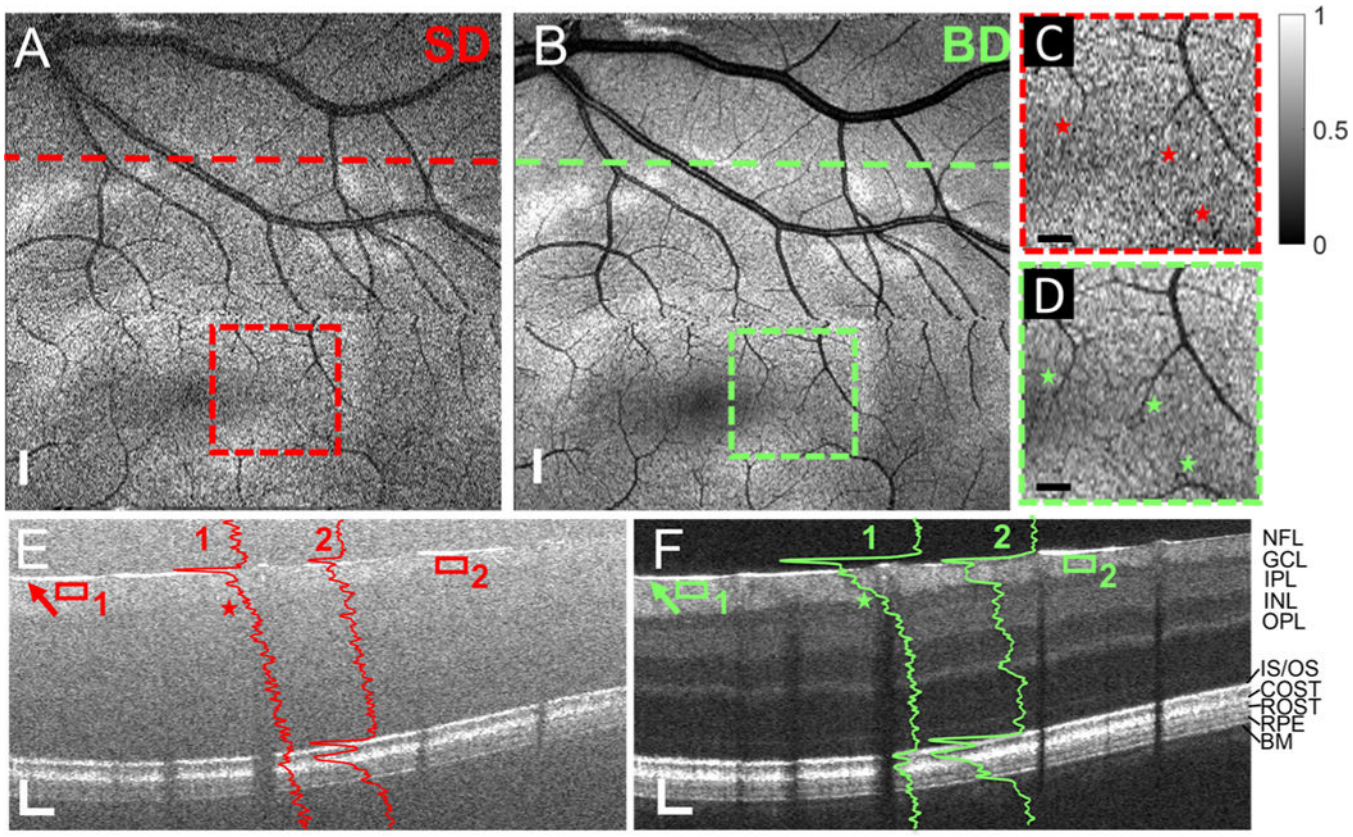

Fig. 5.

Small field-of-view vis-OCT images of the retina of a healthy 47-year-old male (Eye 1); (A) En-face image near the fovea for SD; (B) En-face projection near the fovea for BD; (C) Magnified view of area highlighted by the red dashed box in panel A; red stars highlight small blood vessels; (D) Magnified view of the area highlighted by the green dashed box in panel B; green stars highlight small blood vessels; (E) B-scan image from the location highlighted by the dashed line in panel A; (F) B-scan image from the location highlighted by the dashed line in panel B; Red and green A-lines overlay their respective locations; stars near A-line 1 highlight blood attenuation; red and green arrows highlight locations of PSNFR and PSNR measurement; solid red and green boxes highlight locations of CNR measurement. Scale bars in (A) & (B) are 275 μm (isometric); scale bars in (C) & (D) are 150 μm (isometric); scale bars in (E) & (F) are 60 μm (vertical) × 225 μm (horizontal). NFL: nerve fiber layer; GCL: ganglion cell layer; IPL: inner plexiform layer; INL: inner nuclear layer; OPL: outer plexiform layer; ELM: external limiting membrane; IS/OS: inner segment/outer segment; COST: cone outer segment tips; ROST: rod outer segment tips; RPE: retinal pigment epithelium; BM: Bruch's membrane.

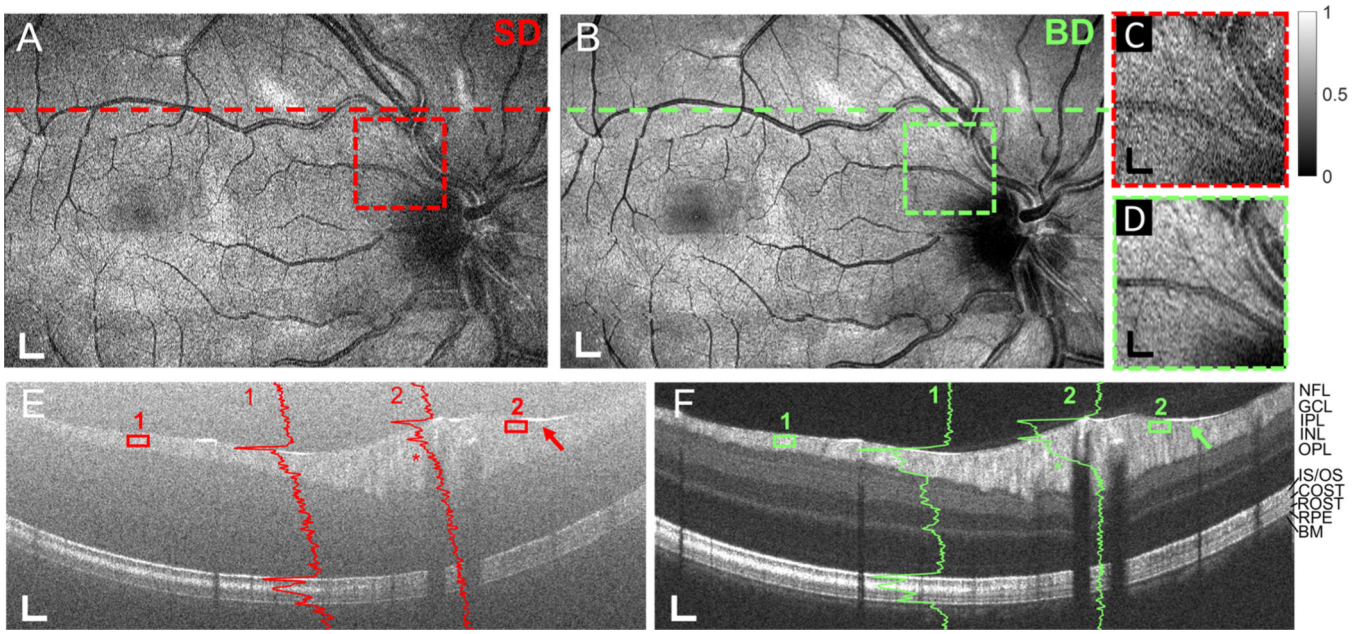

Fig. 6.

Medium FOV vis-OCT images of the retina of a healthy 24-year-old male (Eye 2); (A) En-face image near the fovea for SD; (B) En-face image near the fovea for BD; (C) Magnified view of the region highlighted by the red dashed box in panel A; (D) Magnified view of the region highlighted by the green dashed box in panel B; (E) B-scan image from the location highlighted by the dashed line in panel A; (F) B-scan image from the location highlighted by the dashed line in panel B; Red and green A-lines overlay their respective locations; stars near A-line 2 highlight blood attenuations; red and green arrows highlight locations of SNFR measurement; solid red and green boxes highlight locations of CNR measurement. Scale bars in (A) & (B): 275 μm (vertical) × 325 μm (horizontal); scale bars in (C) & (D): 150 μm (vertical) × 175 μm; scale bars in (E) & (F): 50 μm (vertical) × 275 μm (horizontal).

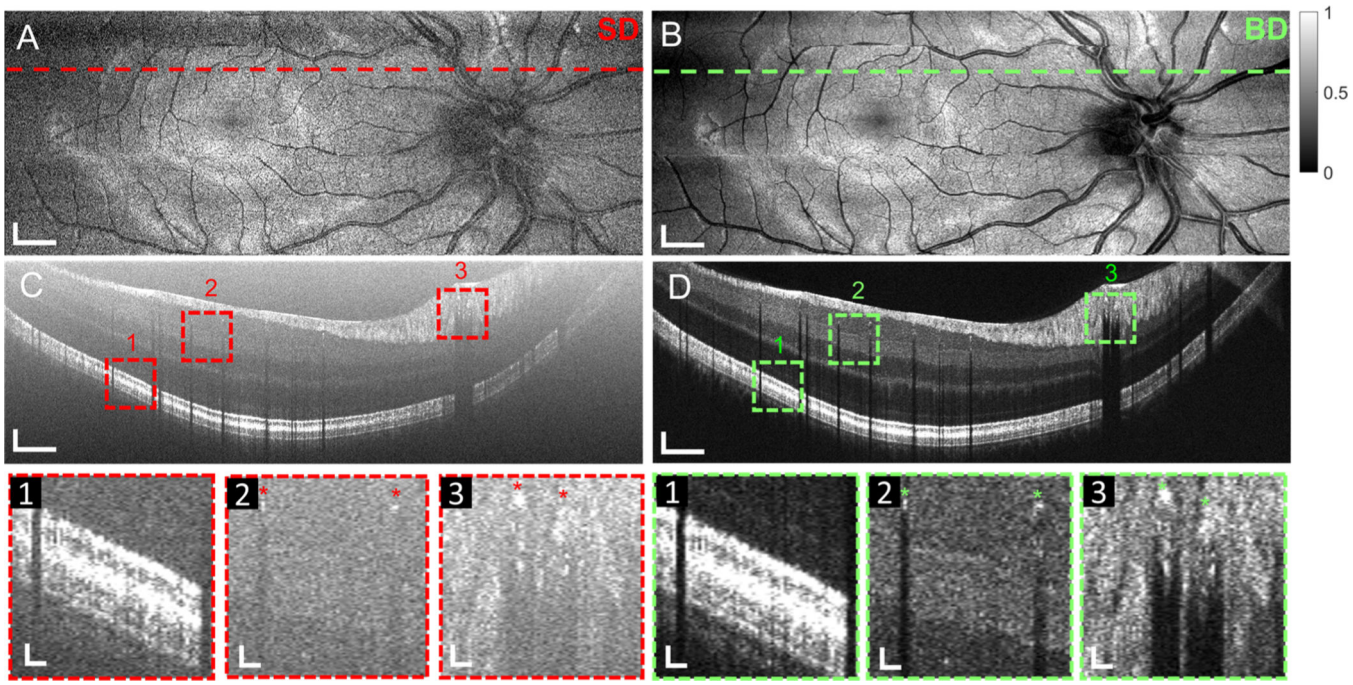

Fig. 7.

(A-D) Large FOV scans in 24-year-old male (Eye 2); (A) En face projection for SD; (B) En face projection for BD; (C) High-density speckle reduction (HDSR) scan at location of red dashed line in (A); (D) High-density speckle reduction (HDSR) scan at location of green dashed line in (B). Red and green dashed boxes in (C) & (D) labeled 1–3 highlight regions for magnification in SD and BD, respectively. Magnifications for respective boxes are shown below. Red and green stars in boxes 1 & 2 highlight blood vessels. Scale bars in (A) & (B): 350 μm (vertical)× 500 μm (horizontal); scale bars in (C) & (D): 100 μm × 700 μm; scale bars in magnification boxes 1–3: 40 μm × 100 μm.

TABLE I

Image Quality Metrics for Phantom Imaging

Image	Method	PSNFR (dB)	PSNR (dB)	CNR 1 (dB)	CNR 2 (dB)	CNR 3 (dB)
Phantom, High Amp.	SD	13.9	26	0.3	1.5	0.3
Phantom, High Amp.	BD	28.7	40.6	3.3	3.9	3.7
Difference SD → BD		14.8	14.6	3.0	2.4	3.4
Phantom, Low Amp.	SD	5.3	17.2	NFL	−7.2	NFL
Phantom, Low Amp.	BD	30.6	42.8	3.4	3.8	3.6
Difference SD → BD		25.3	35.6	NFL → 3.4	11	NFL → 3.6

SD: Single Detection; BD: Balanced Detection; NFL: Noise Floor Limited

TABLE II

Image Quality Metrics for In Vivo Imaging

Image	Method	Scan	PSNFR (dB)	PSNR (dB)	CNR 1 (dB)	CNR 2 (dB)
Eye 1	SD	Small FOV	11.1	23.7	−6.0	−3.8
Eye 1	BD	Small FOV	26.2	38.8	4.4	3.7
Difference SD → BD			15.1	15.1	10.4	7.5
Eye 2	SD	Med. FOV	16.1	28.6	−6.7	−9.7
Eye 2	BD	Med. FOV	31.8	43.8	3.4	3.8
Difference SD → BD			15.7	15.2	10.1	13.5
Eye 3	SD	Small FOV	1.4	12.8	NFL	−6.1
Eye 3	BD	Small FOV	15.5	28.1	4.0	3.0
Difference SD → BD			14.1	15.3	NFL → 4.0	9.1
Eye 4	SD	Med. FOV	8.1	20.9	NFL	−6.6
Eye 4	BD	Med. FOV	22.5	35	1.3	1.2
Difference SD → BD			14.4	14.1	NFL → 1.3	7.8
Eye 5	SD	Med. FOV	8.7	21.3	NFL	NFL
Eye 5	SD	Med. FOV	22.3	35.1	2.2	2.1
Difference SD → BD			13.6	13.8	NFL → 2.2	NFL → 2.1

SD: Single Detection; BD: Balanced Detection; NFL: Noise Floor Limited; Eyes 3–5 shown in Supplementary Materials